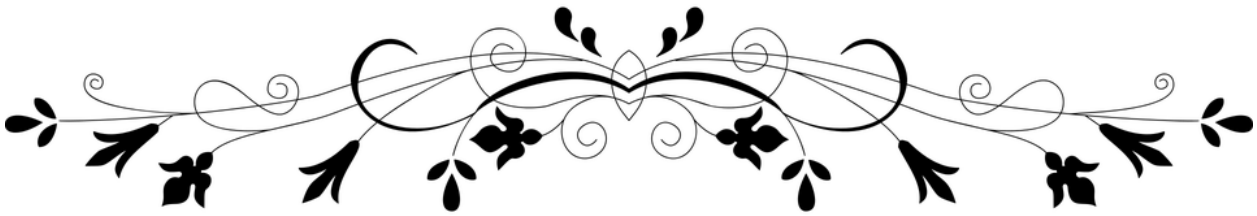

CHAPTER 3

Development of Luminescent Atacamite Nanoclusters for Bioimaging and Photothermal Applications

CHAPTER 3

3.1 Introduction

Atacamite [Cu_2 $(OH)_3$ Cl], is one of rare copper biominerals [121], under investigation in this study, which was anciently discovered from the jaws of marine worm Glycera dibranchiata [139]. It has been considerably explored in diverse applications due to its distinct physicochemical and crystallographic properties [136, 137] besides frustrated magnetism [138]. Despite of being biological origin, its application in the field of biomedical engineering (especially cancer theranostics) has not been investigated yet, the reason being adopted synthetic routes involving use of toxic as well as corrosive chemicals and formation of several microstructural dimensions. Further simultaneous functionality of these synthesized Atacamite structures in diverse physicochemical sectors are also limitedly examined.

By reducing the size of material upto nanocluster level ($\leq$ 2 nm) astounding optical emission, improved catalytic as well as magnetic activity, and discrete optical band gap results [96, 98, 99]. Furthermore nanocluster gained wide attention in the field of bio-imaging as well as cell labelling due to their ultra-small size and better biocompatibility [93] besides high fluorescent quantum yield, and emission tunability. Particularly size reduction in case of semiconductor nanoclusters lead to widening of band gap, modulation of optical absorption energy [244], thus multifaceted applications can evolved.

Therefore it is very much inevitable to investigate the variation in physicochemical characteristics of Atacamite under nanocluster dimension for its probable biological and diverse physicochemical applications. The specific applications in cancer biology also supported from the fact that, effective interaction of glutathione in cancer cell lines with

copper core [245-247] of Atacamite, facilitates their easy cellular uptake. Further, all these applications are also directly related to the light absorption property and electronic band-gap of Atacamite nanoclusters, which need to be studied carefully.

As far as multifunctional biological and other physicochemical applications concerned, biomimetic mineralization [236] put forward an excellent green synthesis approach [248]. Biomimetic mineralization simulates the natural mineralization process by synergistic combination of inorganic and substances. Further it produces nanomaterials with controlled size, morphology, and properties. Plant extract rich in nucleating/stabilizing agents [205] (e.g. polyphenolics, flavonoids, fatty acid esters) under hydrothermal reaction conditions replicate the natural mineralization process in a cost effective manner probably produce Atacamite nanocrystals by suitably selecting process parameters. Most importantly hydrothermal reaction produces nanostructures with excellent crystallinity and surface defects [241]. These surface defects are known to serve as a possible heat-generating site during light exposure [243], thus can be effectively employed for advanced treatment of tumor tissues.

Hence the objective of this study is to suitably select carry out the biomineralization process by employing plant extract to produce nanoclusters of Atacamite in a facile manner. Further evaluation of these small sized nanocrystals for their multifaceted use in various scientific applications. The specific applications currently under investigation in this study mainly comprise of possible bioimaging and photothermal usage of the synthesized nanocrystals. Apart from this the other area of applications include investigation regarding the optical band structure, magnetic activities etc. for boosting the diversification in cancer theranostics.

3.2 Experimental

3.2.1 Synthesis and Silica Encapsulation of Atacamite Nanoclusters

The *M. oleifera* leaf extract (pH ~ 3.5) was prepared by washing the leaves with DI water (18 MΩ.cm), followed by boiling in 100 mL of DI water at 90 ºC for 2-3h, and subsequently, filtered using Whatman 1 filter paper. $CuCl_2.2H_2O$ (> 98.5% Merck Specialties Pvt. Ltd., India) solution (10 mM) was prepared in the DI water and mixed vigorously with 15 mL of freshly prepared *M. oleifera* extract. The prepared suspension was transferred to the Teflon lined stainless steel autoclave and allowed to react for 3h at 120 ºC, under constant stirring. After completion of reaction, the solution was cooled down to room temperature, which was followed by filtration through the Amicon 100 kDa spin columns (Merck Millipore Ltd. Ireland). The collected filtrate contained fluorescent Atacamite nanoclusters (FANC), which was used for further characterization.

The modified StÖber's process was adopted for silica encapsulation of prepared FANC. Typically, 10 mL of DI water, 30 mL of absolute ethanol (> 99.8%, Honeywell, Germany), 1.4 mL ammonia solution (25%, SRL Chemicals, India), 100 µL of Aminopropyl triethoxysilane (APTES) (> 98%, High Media Labs, India) and 50 µL of Tetraethyl orthosilicate (TEOS) (> 99%, Sigma-Aldrich, USA) were mixed thoroughly at room temperature followed by the addition of 9 mL suspension of FANC under vigorous stirring. The mixture was transferred to a Teflon lined autoclave and allowed to react for 12 h at room temperature. After completion of reaction, the solution was centrifuged at 15000 RPM for 5 min, and the supernatant was collected. This solution contains silica encapsulated fluorescent Atacamite nanoclusters (SEFANC).

3.2.2 Characterization

The X-ray diffraction (XRD) (Rigaku Smart Lab diffractometer) technique (radiation source: CuKα; scanning rate: 3.03 °/min) was used to analyze the phases present in the developed nanoclusters. The size and particle distribution were examined using transmission electron microscopy (TEM, FEI TECNAI G^2 20 TWIN). The thermogravimetric analysis (TGA) and differential scanning calorimetry (DSC) were carried out using NETZSCH STA 449 F3 instrument. During the analysis, ~5.39 mg of the sample was heated from room temperature to 800 °C at a heating rate of 10 °C/min. The nitrogen was chosen as carrier gas with a constant flow rate of 10 mL /min. The valency of FANC/SEFANC atoms were ascertained by x-ray photoelectron spectroscopy (XPS) (AMICUS, Kratos Analytical). The organic functionality on FANC/ SEFANC was analyzed using FT-IR spectrometer (Thermo Electron Corporation, USA). The absorbance analysis were carried out with liquid samples using UV-VIS Spectrophotometer (SL-159, ELICO, India) in the spectral range of 280-1000 nm. The fluorescence spectra of leaf extract/FANC/SEFANC was acquired with the help of a spectrofluorometer (QM-400 HORIBA Canada, *Appendix* A1). Fluorescence decay measurements were carried out using Edinburg Instrument. Mass fragments were analyzed by electrospray ionization mass spectroscopy (ESI-MS) (Shimadzu, Japan). The magnetic property of prepared nanoclusters was evaluated with the help of squid based magnetometer (MPMS, Quantum Design Inc. USA).

3.2.3 Quantum Yield Measurement

The relative quantum yield of FANC or SEFANC was evaluated with respect to quinine sulfate dihydrate (High Media Lab, India). A standard curve was plotted between integrated fluorescence intensity value with respect to absorbance (< 0.1) for different

quinine sulfate dihydrate solution concentrations, prepared in 0.1 M H_2SO_4. A similar procedure was also followed in the case of SEFANC and FANC suspension with DI water, acting as diluents. The slope, obtained from the linear fitting of the standard curves, was used to calculate the quantum yield using equation 1.

$$\Phi x = \Phi st \times \frac{Gradx}{Gradst} \times \frac{\eta 2x}{\eta 2st} \quad (1)$$

Φ_x = Quantum yield of FANC or SEFANC

Φ_{st} =Quantum yield of standard

$Grad_x$= Gradient of curve plotted for FANC or SEFANC

$Grad_{st}$= Gradient of curve plotted for standard

η_x = Refractive index of solvent used for preparing FANC or SEFANC solution

η_{st}= Refractive index of solvent used for preparing quinine sulfate standard

The quantum yield of quinine sulfate dihydrate has been estimated to be 0.54 [249]. The refractive index for 0.1M H_2SO_4 was taken to be 1.3.

3.2.4 MTT Assay

The 3-(4, 5-dimethylthiazol-2-yl)-2,5diphenyltetrazolium bromide (MTT) (Thermofisher, USA) assay was performed to measure the cytotoxic effect of SEFANC on Drosophila (Wild type) salivary gland tissues. The salivary glands were dissected from third instar larvae in phosphate buffer saline (1X PBS). The tissues were incubated with different concentrations (0.1 mg/mL to 0.5 mg/mL) of SEFANC for 45 min at room temperature, while control was incubated with 1X PBS for a similar duration. After incubation, the tissues were washed twice with 1X PBS and incubated with 100 µL of MTT (0.6 mg/mL) in each well for 2h at 37 ºC. Subsequently, the MTT was removed,

and the 200 µL DMSO (> 99% Merck Specialties Pvt. Ltd., India) was added and kept for 1h at 37 ºC to dissolve the purple formazan crystals. The absorbance was taken at 570 nm with Synergy H1 Hybrid multimode plate reader. The results were interpreted as percent cell viability, as compared to the control samples.

3.2.5 Fluorescence Imaging of Drosophila Salivary Gland Tissue

Wild type (Oregon-R^+) Drosophila 3rd instar larvae were dissected out with the help of fine needles under the stereo-zoom-microscope to isolate the salivary glands in 1X PBS. In one set- salivary glands were incubated with SEFANC (0.5 mg/mL) for 45 min at room temperature while another set, incubated with 1XPBS, was considered as control. After incubation, tissues were quickly washed twice with 1X PBS, and the respective samples were mounted in 1XPBS which was followed by fluorescence imaging. The images were captured with Nikon Ni-U fluorescence microscope using DAPI filter- Ex-340-380, DM 400, BA 435-480. The fluorescence intensity profiles of respective samples were measured using Nikon-NIS-element BR software.

3.2.6 Viability of MG-63 Cells and Photothermal Efficacy

The viability of osteosarcoma (cancerous tumor in bone) MG-63 cells, incubated with SEFANC, were examined using MTT assay. Prior to MTT assay, MG-63 cells were cultured in Dulbecco's modified Eagle's medium (DMEM) (Sigma Aldrich, USA), supplemented with 15 % fetal bovine serum (FBS) (Sigma Aldrich, USA) and 1 % antibiotics (Sigma Aldrich, USA), and incubated under humidified CO_2 (5 %) atmosphere at 37 ºC. After achieving 70-80% confluency, the cells were trypsinized and the equal amount of cells (10^4 cells/mL) were seeded in 24 well plates and incubated for another 24 h. After 1 day of incubation, culture media in each well was replaced by fresh media containing 100 µL of SEFANC (0.1-0.5 mg/mL) and incubated for another 4 h.

Control sample was incubated for similar duration in presence of only growth media. Two batches of SEFANC treated MG-63 cells were prepared: one batch was exposed to 975 nm radiation (diode laser) for 5 min and the other was kept in dark (no irradiation). The photothermally treated and untreated (control) cells were used for IC_{50} analyses. Furthermore, bright-field images of photothermally treated cells and control were obtained by Nikon Ni-U fluorescence microscope.

After incubation process, the cells were washed with 1X PBS and again incubated with 500 µL reconstituted MTT (5 mg/mL MTT in 1X PBS) and DMEM with 1:10 dilution for 6 h to form formazan crystals. The purple colored crystals were dissolved in DMSO and absorbance was recorded at 590 nm using ELISA microplate reader (Bio-Rad iMark TM). The results were interpreted as percent cell viability as compared to the control. Statistical analysis were carried out with two way ANOVA technique using GRAPHPAD PRISM software.

Before SEFANC irradiation, the photo-generated heat was measured by introducing 200µL FANC or SEFANC suspension into a tubular quartz sample holder, fixed with a K-type thermocouple and a temperature indicator. The suspension was exposed to 975 nm radiation using inexpensive continuous wave diode laser. The laser was operated at 500 mW power with a beam spot size of $\leq$ 2.5 mm x 5.2 mm, focused on the sample. The increase in temperature with time was recorded continuously. Similar experiments were carried out for DI water (no FANC) using pure silica nanoparticles as control. The change in temperature (ΔT) after NIR exposure were calculated. For different SEFANC concentrations, ΔT was also evaluated. The thermal stability was examined by exposing a fixed concentration (0.5 mg/mL) of SEFANC to 975 nm radiation. The same procedure was repeated thrice.

3.3 Characterization & Property Evaluation

3.3.1 Characterization of Atacamite Nanoclusters

The size of the Atacamite was ascertained by transmission electron microscopy (TEM) as shown in Figure 3.1. TEM image revealed the formation of well separated nodular shaped (Fig. 3.1a) nanoclusters of size ~1.9 nm in size (Fig. 3.1c), comprising of sub-clusters (Fig. 3.1b) of size ~ 0.7 nm (Fig. 3.1d).

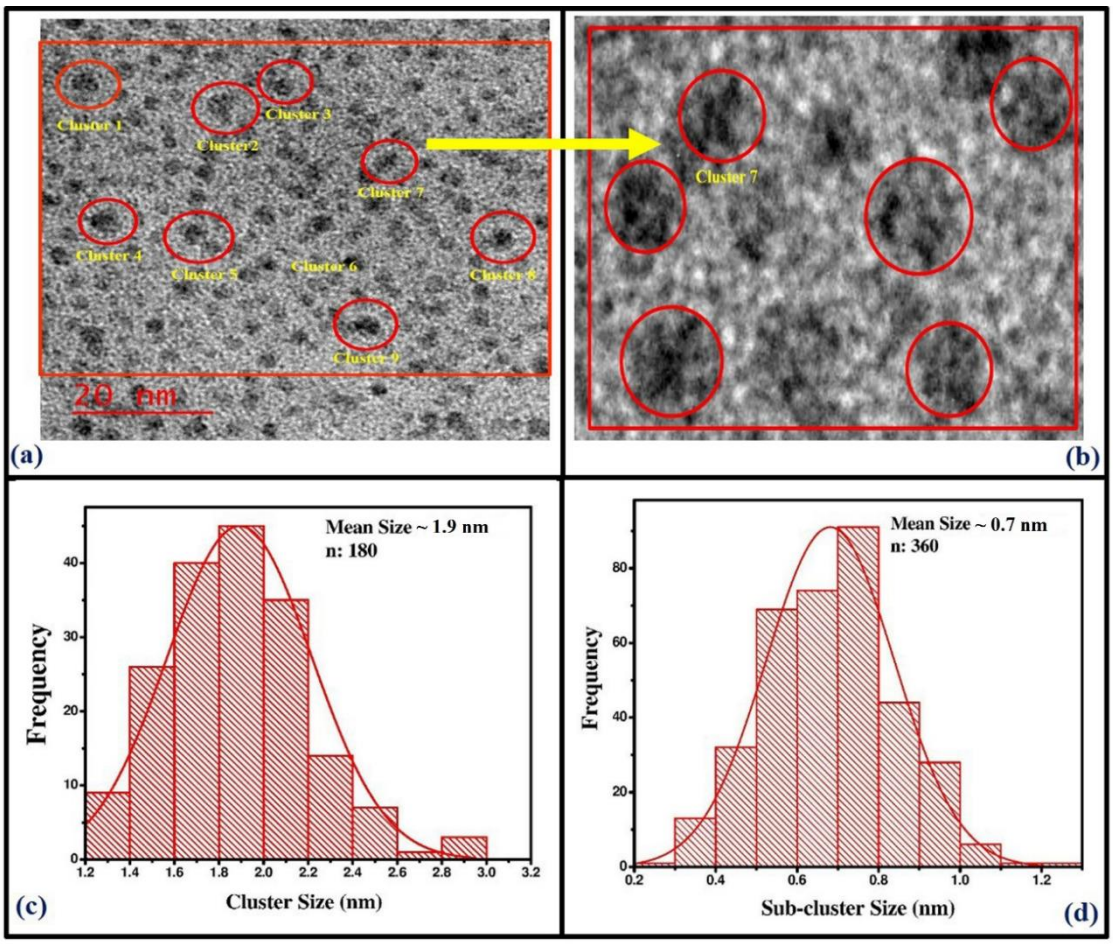

Figure 3.1 (a) TEM images of monodispersed FANC. (b) Closure view image of single FANC, consisting of different sub clusters. (c) Size distribution histogram of nanoclusters in FANC represented (d) Sub-nanoclusters size distribution, constituting the nanoclusters.

The XRD pattern of FANC (Fig. 3.2a) revealed the formation of Atacamite crystals (primitive orthorhombic; a =6.03 Å, b=6.86 Å and c= 9.12 Å), confirmed by standard

crystallographic pattern of the pure Atacamite mineral (American Mineralogist crystal structure data base, RRUFF ID: RO50098.1) [131].

The TGA profile revealed three continuous regions: 30-110 ºC, 110-400 ºC and 400-700 ºC. The slight depression in TGA profile between 30-110 ºC may be attributed to the unbound moisture release, followed by a rapid mass loss due to dehydration and dehalogenation between 110-400 ºC and 400-700 ºC, respectively (Fig. 3.2b). These results were further corroborated by the presence of two broad endothermic peaks in the DSC profile within above mentioned temperature range. These peaks indicate dehydration and dehalogenation of Atacamite to cupric oxide as shown by following reaction scheme 2 and 3 [250] as,

$$2Cu_2(OH)_3Cl \longrightarrow CuO.CuCl_2 + 2CuO + 3H_2O \quad (2)$$

$$CuO.CuCl_2 + ½\ O_2 \longrightarrow 2CuO + Cl_2 \quad (3)$$

Thermal decomposition behavior obtained from TGA/DSC corroborates the results, obtained from XRD indirectly.

To confirm the presence of various functional groups on FANC, Fourier transform infrared spectroscopy of the Atacamite powder was performed. The FTIR data (Fig. 3.2c) revealed the presence of five major bands, centered at ~3500 cm^{-1}, ~1722 cm^{-1}, ~1620 cm^{-1}, ~1396 cm^{-1} and 1080 cm^{-1} indicating probable presence of R-NH_2 (primary amine)/ OH stretching, C=O, C=C, methoxy, C-O stretching and vibration bands, respectively. Moreover, these FTIR bands indicate the presence of proteins, polyphenolics, cyclic acids, ethers, ester, methoxyl substituted aromatic acid, and pyrolic compounds on the FANC surface. The medium intense transmittance peak below 1000 cm^{-1} (finger print region) is mainly due to metal oxide bonds arising from inter atomic vibrations [233].

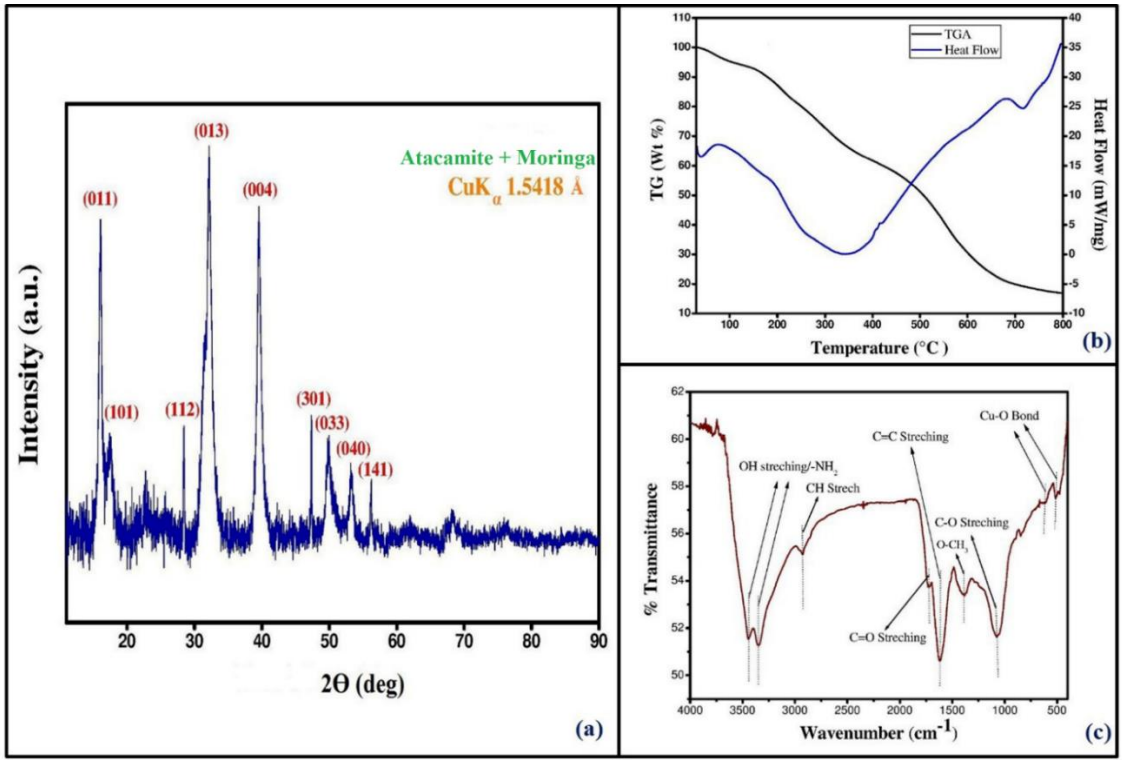

Figure 3.2 (a) XRD pattern of the FANC powder (b) Thermogravimetric and differential Scanning calorimetry spectra for FANC powder. (c) FTIR spectra of FANC.

In the case of FANC, transmittance peaks near ~500 cm^{-1} and ~600 cm^{-1} are largely due to Cu-O bond in Atacamite structure [137]. The FTIR bands, ranging from 3300-3600, 1600-1650 cm^{-1}, and values below 900 cm^{-1} have been reported to result from hydroxyl group, associated with –OH stretching vibration, surface adsorbed water, and metal-oxygen lattice interaction, respectively [140]. These findings support the formation of Atacamite. Furthermore, detailed X-ray photoelectron spectroscopy (XPS) was carried out to understand the oxidation state of different elements, involved in the formation of Atacamite.

The XPS spectra were acquired for Cu, O, Cl, and C, elements, deconvoluted and presented with 1.6 eV offset correction to major and satellite peak binding energies, which is accountable, for the instrumental shift in carbon peak (286.4 eV) [251, 252] (Fig. 3.3a). The copper XPS spectra (Fig. 3.3b) displayed two major peaks, centered at

936.28 and 955.68 eV, which correspond to the binding energies (B.E.) of Cu $2p_{3/2}$ and Cu $2p_{1/2}$ orbitals. In addition to these peaks, two shake up satellite peaks, centered at 945 and 965.1 eV are also observed, attributing to the involvement of $2p_{3/2}$ and $2p_{1/2}$ orbitals, respectively. These peaks confirmed Cu^{+2} oxidation state, mainly due to presence of copper hydroxide linkage [125, 253]. Shakeup satellites peaks are characteristics of the compounds, with Cu^{+2} ions. However, due to close resemblance with relative intensity of Copper oxide, the formation of a smaller amounts of CuO on FANC surface cannot be ruled out [254, 255].

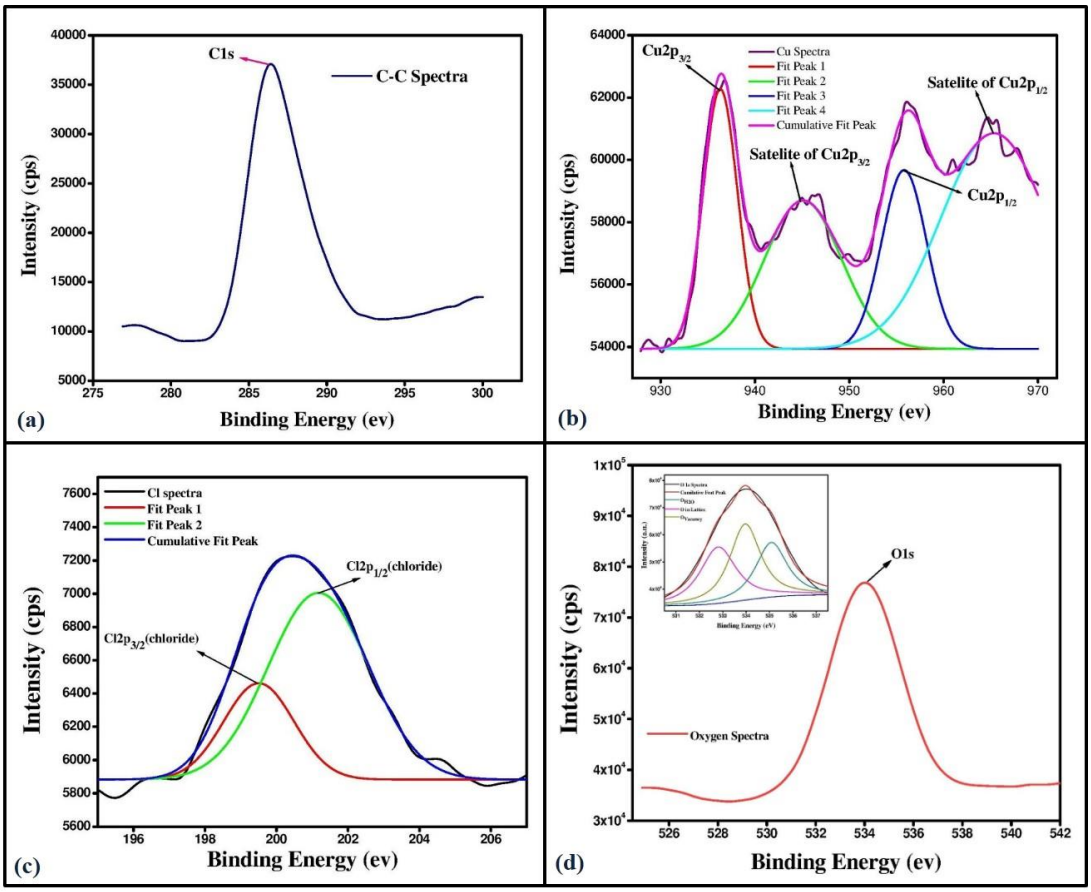

Figure 3.3 XPS spectra of (a) C 1S electrons (b) Cu 2p electrons in FANC (c) Cl 2p electrons in FANC and (d) O 1s electrons (inset shows deconvoluted spectra).

The deconvoluted spectra of chlorine (Fig. 3.3c) revealed two shifted satellite peaks at 199.5 and 201.1 eV, corresponding to binding energies of Cl $2p_{3/2}$ and Cl $2p_{1/2}$ orbitals,

which can be attributed to the formation of Cu-Cl bond. The peak, centered at 534 eV corresponds to the O 1S orbital (Fig. 3.3d), is slightly shifted, which is probably associated with the carbonate contamination [256] during hydrothermal synthesis [233]. This feature is also reflected in case of copper spectra where Cu $2p_{3/2}$ peak is slightly shifted towards higher binding energy. Moreover, the single O 1S peak can be deconvoluted into a three Gaussian peaks (Fig. 3.3d inset) at about 532.8 eV, 533.9 eV, and 535 eV, attributing to lattice oxygen, surface defects and adsorbed oxygen, respectively [125]. Moreover, overall XPS analyses revealed the formation of Atacamite, which was also previously verified through TGA and FTIR.

3.3.2 Optical Properties of Atacamite Nanoclusters

Figure 3.4b shows fluorescence output from control and Atacamite nanocluster suspensions. Initially, cluster containing suspension was scanned to obtain an excitation maximum of 350 nm. Upon 350 nm excitation, a broad emission (400-650 nm) spectrum with peak maxima at 460 nm (Fig. 3.4a) was observed. A weak and slightly red-shifted emission (~2 nm) from FANC was obtained as compared to the control. Furthermore, life-time measurements (*Appendix* A2) of control (τ =1.99 ns) and nanoclusters (τ =2.1 ns) were found to be almost similar (Fig. 3.4c), indicating the emission from the same source, in both the cases. According to the published reports, naturally existing fluorophores are known to be short lived (0.1-5 ns) [257]. After 13 days of shelf-life, the fluorescence intensity of FANC was observed to decrease by 30% (Fig. 3.4d). This decrease in intensity can be attributed to masking of ligands by developed oxide layer, catalyzed by surface defects on FANC. The formation of Copper oxide also has been confirmed by the improved light absorption in 600-1000 nm region by FANC.

3.3.3 Atacamite Nanoclusters Band Gap Analysis

The probability of band edge emission in clusters [258] was verified through Tauc plot, obtained using absorbance spectra of FANC. The linear region of Tauc plot was extrapolated, and intercept was calculated. The band gap values of about 3.9 and 2.5 eV (*Appendix* A3), corresponding to direct and indirect band gap nature of prepared nanoclusters. Such type of dual band gap nature may be attributed to the imperfect crystallinity in the developed nanostructures [259]. The band gap value of Atacamite has not been previously reported and therefore, the polymorphs of copper hydroxy chloride were used for comparison. The slight reduction in Atacamite indirect bandgap value as compared to Paratacamite is likely due to the substitution of some phytochemicals in the Atacamite lattice sites [260]. Generally, crystal momentum vector of a carrier in the lowest state of conduction band significantly differs from that in highest state of valence band of an indirect bandgap semiconductor. Due to which, electron-hole recombination does not take place and therefore no radiative decay occurs. However, the absorbed energy is converted into phonons, which results in heat generation. Additionally, Atacamite exhibits a direct band gap of 3.9 eV. The band edge value, corresponding to valence and conduction bands of prepared Atacamite nanoclusters was evaluated from the following equations,

$$E_{VB} = X - E + 0.5E_g \quad (4)$$

$$E_{CB} = X - E + 0.5E_g \quad (5)$$

$E_{CB/VB}$ = Lower and upper band edge of conduction and valence bands, respectively

X = Absolute electronegativity

E = Energy of free electron on hydrogen scale

E_g= Calculated band gap of material

Using equations 4 and 5, a band edge of 0.9 (E_{CB}) and 3.4 eV (E_{VB}) have been obtained.

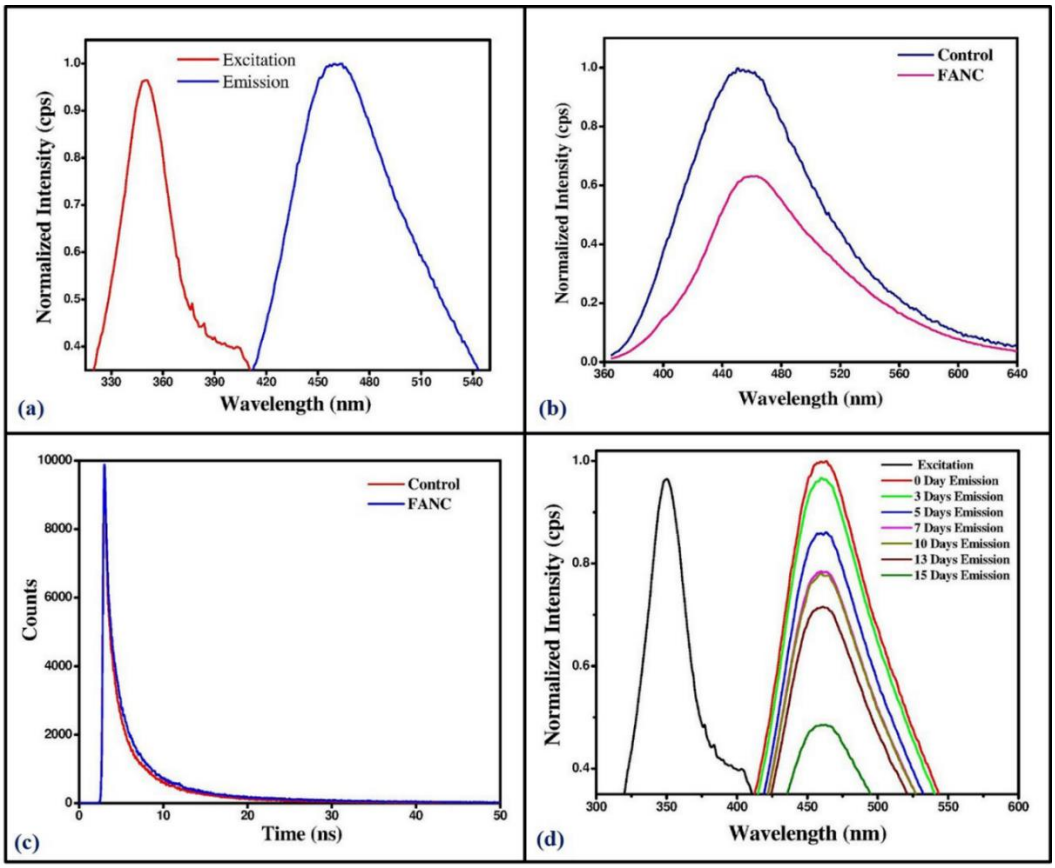

Figure 3.4 (a) Excitation and emission spectra of FANC (b) Emission from FANC and control (c) Fluroscent lifetime decay curve of control and FANC (d) Effect of shelf life on emission property of FANC and SEFANC.

3.3.4 Design of Fluorescent Atacamite Nanoclusters

Semiconducting Paratacamite, a polymorph of Atacamite, is known to have an indirect band gap of (E_g) = 2.65 eV. It is noteworthy that Atacamite nanoclusters have been obtained to exhibit an indirect band gap of 2.5 eV, which is similar to that of Paratacamite. Also, it is well known that indirect band gap material does not show fluorescence. Therefore, it is required to impart fluorescence to enable bioimaging application, by externally incorporating fluorescent ligands on FANC surface. Early studies, rendering

non-fluorescent nanoclusters fluorescent by conjugating or physically adsorbing fluorescent dyes have been extensively reported [261-264]. However, these strategies require the use of expensive fluorescent dyes, conjugating linkers, reagents, and additional purification steps. Direct attachments of naturally existing fluorescent ligands in the plant extract on the surface of Atacamite nanoclusters by hydrothermal method excludes the high cost and complexity involved in conjugating fluorescent dyes on nanoclusters surface. *M.oleifera* leaf extract is observed to be fluorescent (Fig. 3.4b) due to naturally existing fluorophores such as flavonoids and chlorophyll pigments [265]. Also, these ligands are observed to be in higher content in *M.oleifera* leaf extract as compared to other medicinal plants commonly found in India [229]. During synthesis, these organic ligands automatically get attached on FANC surface, which has been previously confirmed by FTIR analysis (Fig. 3.2c). Furthermore, the number of Atacamite molecules, associated with the nanoclusters and their ligands was estimated using electron-spray ionization-mass spectrometry (ESI-MS).

3.3.5 ESI-MS Analyses

Such soft ionization technique (ESI-MS) is capable of analyzing organic fragments as large as 2 kDa. The ESI-MS spectra (*Appendix* A4) was obtained in positive scanning mode. The peaks corresponding to m/z value of 545.4, 501.37, 457.34, 425.21, 413.26, 403.23 and 381.3, probably attributed to $[(Cu_2(OH)_3Cl)_2 + Catechol]^+$,$[(Cu_2(OH)_3Cl) + Kaempferol]^+$/ $[(Cu_2(OH)_3Cl) + Pyrrole]^+$, $[(Cu_2(OH)_3Cl)_2 + Na]^+$, $[(Cu_2(OH)_3Cl)_2]^+$, $[Cu_2(OH)_3Cl + Ascorbic\ Acid + Na]^+$/ $[Cu_2(OH)_3Cl + Syringic\ Acid]^+$, $[Cu_2(OH)_3Cl) + Caffeic\ Acid/Ferulic\ Acid]^+$, $[Cu_2(OH)_3Cl + Gallic\ Acid/Vanillic\ Acid)]^+$ respectively. Mostly, these phytochemicals, associated with nanoclusters, belong to flavonoids (polyphenolics), phenolic acid groups, which are fluorescent in nature. Based on

information obtained from FTIR and ESI-MS analyses, a possible Atacamite nanoclusters synthesis mechanism has been proposed.

3.3.6 Proposed Reaction Mechanism

The possible reaction mechanism for the formation of Atacamite nanocluster is represented in Figure 3.5. The presence of several reducing/stabilizing agents in M.oleifera leaf extracts such as, ascorbic acid, quercetin, and chlorogenic acid under acidic condition are likely to reduce $Cu^{+2} \rightarrow Cu^{+}$ ions which may undergo disproportion reaction to give Cu^{+2} ions, which on further reaction results in the formation of Atacamite.

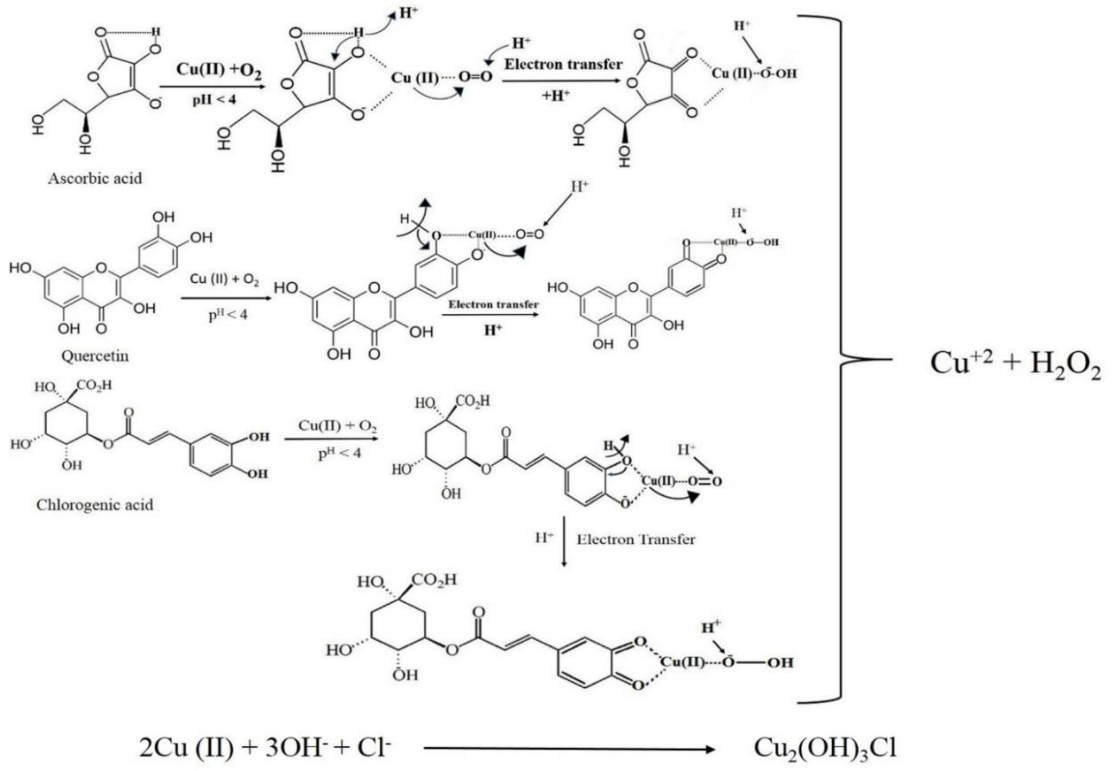

Figure 3.5 Probable reaction pathway for the formation of Atacamite from plant phytochemicals.

Ascorbic acid or quercetin experienced a similar kind of oxidation effect, catalyzed by cupric ion under acidic conditions to produce Cu^{+2} ions [266, 267]. Kasisomayajula et al. [134] have reported a detailed mechanism of formation of Atacamite from redox

catalyzed reaction of polypyrolic compound in presence of cupric ion under acidic conditions.

3.3.7 Silica Encapsulation of FANC (SEFANC)

3.3.7.1 Characterization of SEFANC

The silica encapsulation of FANC was ascertained using high resolution transmission electron microscopy, as shown in figure 3.6a. The HR-TEM image shows complete encapsulation of FANC within silica layer. A closer view of the SEFANC displays dark FANC core confined within light silica layer (Fig. 3.6a). Furthermore, aggregation of several FANC nanoclusters within the silica shell is clearly visible. To ascertain the crystallinity of the SEFANC, XRD studies were carried out.

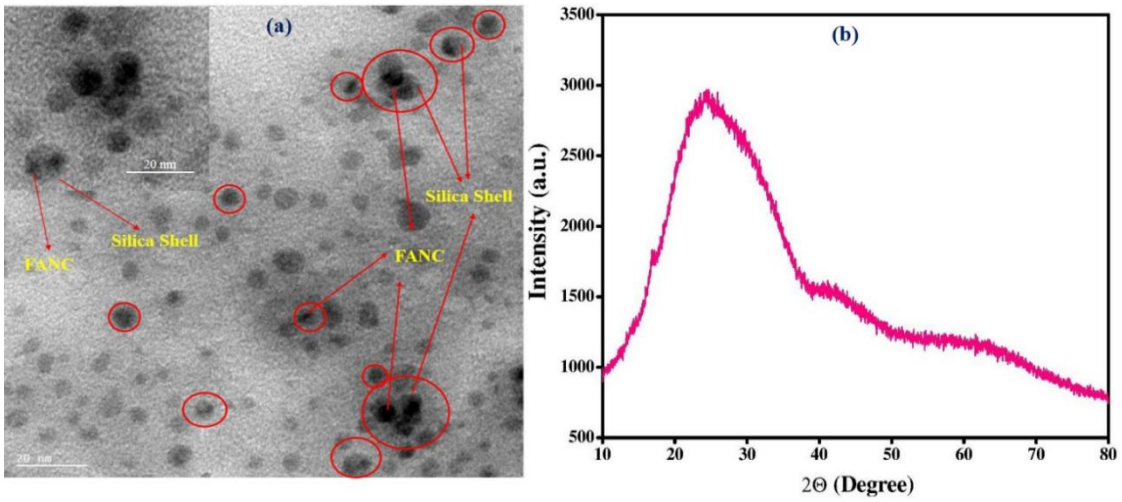

Figure 3.6 (a) HR-TEM image showing complete encapsulation of FANC (dark core) within transparent silica layer. (b) XRD pattern of SEFANC.

The XRD pattern (Fig. 3.6b) of SEFANC shows a single broad peak at ~24^{o} (2θ), which corresponds to surface diposited amorophous silica layer [268]. The formation of dense silica structure indicates complete encapsualtion of Atacamite nanoclusters. However, due to silica encapsulation, the characterisitc Atacamite XRD peaks are masked [269-272]. Further, to obtain the details of valence state of FANC, encapsulated in silica shell,

XPS analyses were performed (Fig. 3.7). The XPS analyses of SEFANC showed O 1s and Si 2p spectra, better resolved than Cu 2p and Cl 2p spectra, due to the large surface contribution from silica layer. The deconvoluted carbon 1s peak resulted into three gaussian peaks, corresponding to the binding energy (B.E.) of 284.7, 286.1 eV and 287. 9 eV. These peaks were associated with C-C, C-O-C, and O-C=O bonds, respectively. The XPS analysis of Cu (Fig. 3.7a) revealed Cu $2p_{3/2}$ and Cu$2p_{1/2}$ peaks at B.E. of ~ 933.9 and 953.3 eV. Whereas, its satellite peaks were observed at the B.E. of about 942.6 and 964.7 eV, indicating Cu^{+2} bonded with hydroxide moiety [125]. The peak at B.E. 932.9 eV indicates the formation of surface CuO layer over the Atacamite nanocluster. Nevertheless, poorly evolved satellite peaks in addition to its main peak suggests encapsulation of small sized nanoclusters within silica layer. Whereas, the Cl $2p_{3/2}$ and Cl $2p_{1/2}$ spectra at ~197.8 and 199.4 eV (Fig. 3.7b) can be attributed to the metal chloride (Cu-Cl) bonding, present in the Atacamite. It is important to note that the XPS spectra of the copper and chlorine in the case of SEFANC are slightly shifted as compared to raw FANC, due to silica encapsulation [273]. Furthermore, the XPS spectra of silica (Si 2p, Fig. 3.7c) shows single gaussian peak at ~ 102.5 eV due to O-Si-O surface bonding [272, 274], indicating dense silica layer formed on the FANC surface. The O1s peak was deconvoluted (Fig. 3.7d) to generate two gaussian peaks at about 532.1 eV associated with surface silica layer and ~534.7 eV resulting from Cu-O bonding in Atacamite.

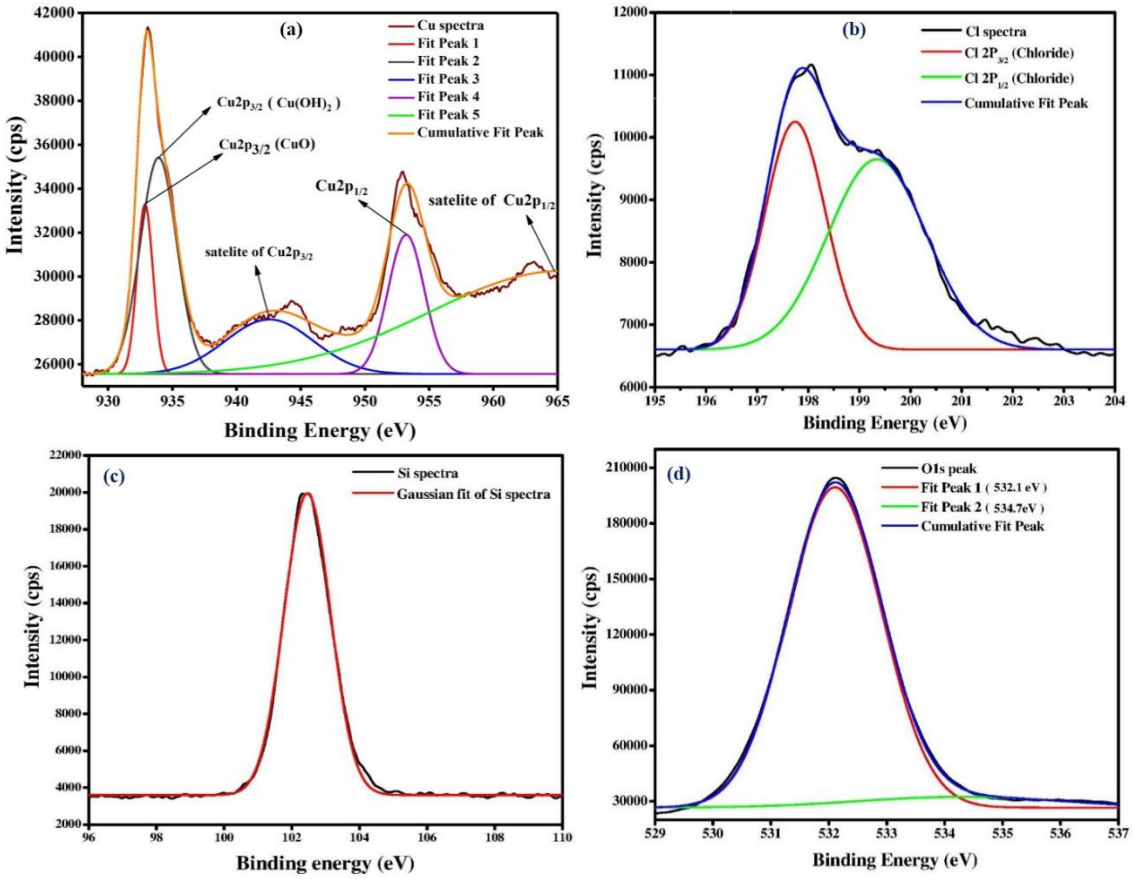

Figure 3.7 XPS spectra of (a) Cu 2p electrons in SEFANC (c) Cl 2p electrons in SEFANC (c) Si 2p electrons (d) O 1s electrons.

The high binding energy value of Cu-O spectra as compared to Si-O-Si can be correlated with higher electronegativity of Cu as compared to Si [272]. It is interesting to note that the higher shift in binding energy value in case of oxygen spectra, both in FANC and SEFANC can be due to Cu^{+2} ion interaction with the surface deposited carboxylate ligand from plant extract [275]. Briefly, XPS results indicates encapsulation of FANC within the silica shell and also indicates slight formation of Copper oxide layer.

Next, FTIR study was used to analyze the formation of silica layer over FANC and associated functional groups (Fig. 3.8). The FTIR spectra of FANC (studied earlier) and SEFANC were found to be overlapping, indicating silica encapsulation of FANC. The broad transmittance peak near ~ 3400 cm^{-1} resulted due OH stretching vibrations of

alcoholic and aqueous precursor used during the silica encapsulation. The early studies [276] demonstrates that the OH stretching vibrations are due to silianol group on the surface of nanostructures. Further, FTIR analyses exhibited peaks at 1030-1180, 930, 680-790, and 450 cm^{-1}. The intense transmittance band in the range of 1030-1180 cm^{-1} and 680-790 cm^{-1} corresponds to Si-O-Si asymmetric and symmetric stretching vibrations respectively, related with TEOS compound [268]. This result indicates the formation of condensed silica layer over encapsulated nanostructure [276]. Whereas, the FTIR peak at ~ 450 cm^{-1} can be attributed to the Si-O bending vibrations associated with Si-O-Si or O-Si-O bond in surface silica layer [277]. It is noteworthy that FTIR peak at about 930 cm^{-1} is due to free Si-OH (silanol group) stretching vibrations, indicating the bonding between FANC and surface silica layer [271], strengthened by the appearance of FTIR peak at ~615 cm^{-1} [269].

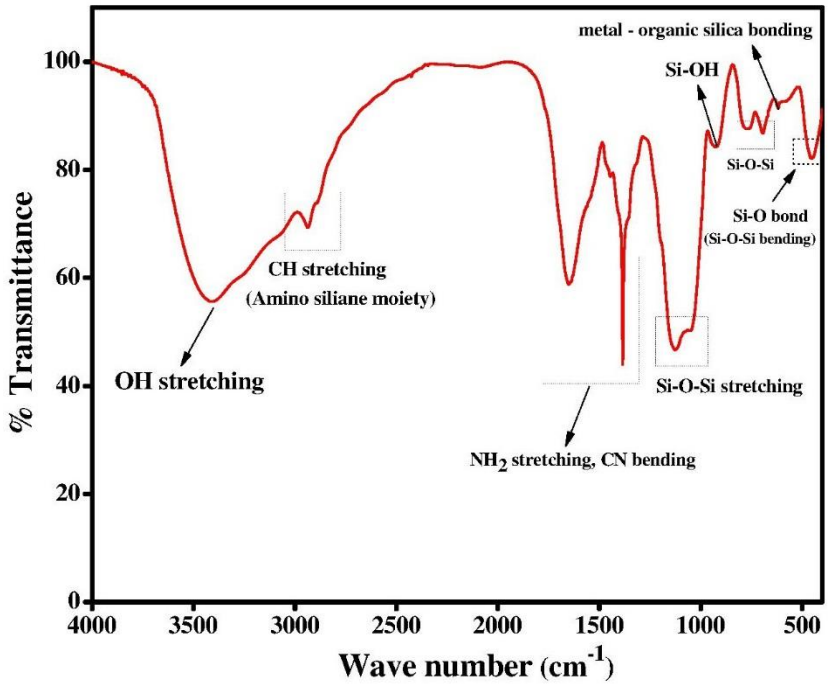

Figure 3.8 Functional group analyses of SEFANC through FTIR spectroscopy.

Further, the FTIR spectra at 1380, 1650, 2870-2930 cm^{-1} represented NH_2 bending, CN stretching and CH stretching vibrations related to APTES [268, 276], indicating presence of amino silane moieties on the surface of SEFANC.

3.3.7.2. Optical Properties of SEFANC

The luminescence quenching of fluorophores, attached to the defective surface of nanoparticles has been reported [278, 279]. It is important to note that hydrothermal synthesis leads to the formation Atacamite nanoclusters with surface defects. These defects can quench the emission of the attached fluorophores. The other reason for quenching could be structural variation in fluorescent ligands when adsorbed on the nanoclusters surface. This can be solved by sterically confining such ligands or defects within the silica matrix, which is an easier and inexpensive method. Silica encapsulation restricts aggregation of nanoclusters and protects ligands or defects from diffusing ions. Early work by Cai et al. [280] has demonstrated significant improvement in GFP fluorescence on silica encapsulation due to increased structural stability. Consequently, FANC was encapsulated with in the silica shell, and confirmed by TEM, XPS and FTIR studies. After silica encapsulation, significant increase in SEFANC fluorescence intensity was observed (Fig. 3.9a), as compared to FANC. Further studies were performed to evaluate the colour emission of SEFANC. The colour chromaticity diagram (CIE) indicated intense blue colour emission from the SEFANC as compared to FANC (Inset, Fig. 3.9a). Moreover, it was also observed that the fluorescence intensity of the SEFANC did not change even after 15 days of storage (4 ºC), a remarkable improvement in FANC (Fig. 3.6b) shelf-life upon silica encapsulation. Besides, it is interesting to note that even after prolonged exposure (1h) to 350 nm light excitation, FANC emission intensity declined only at the rate of 0.15 %/min (Fig. 3.6c) as compared to Rhodamine 6G (quenching rate 0.23 %/min) [249]. The photon conversion efficiency in terms of number

of photons emitted to the number of photons absorbed (quantum yield) [63] by FANC and SEFANC was also evaluated. The results revealed significant increase in relative quantum yield of SEFANC (1.7 %) as compared to the FANC (~0.3%). The relative quantum yield for FANC and SEFANC was calculated with respect to quinine sulfate dihydrate standard.

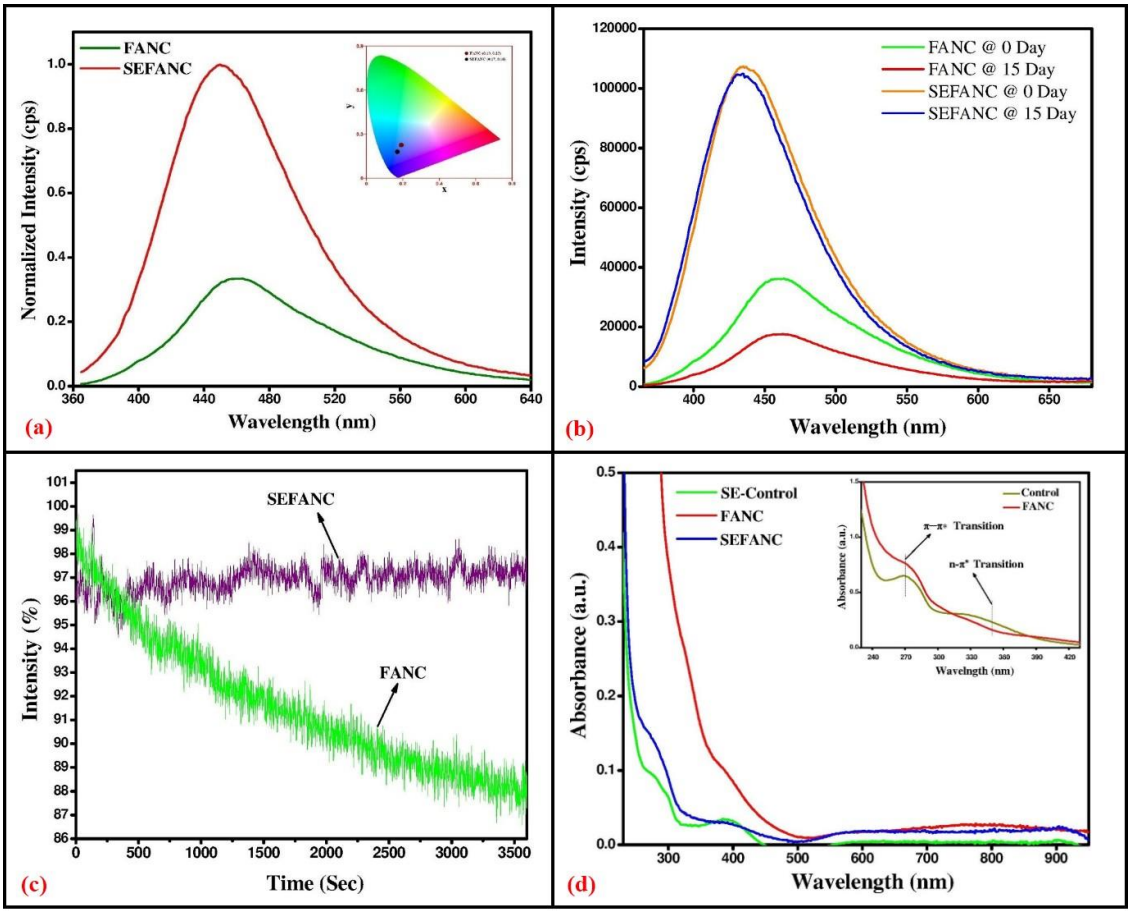

Figure 3.9 (a) Emission spectra for FANC and SEFANC (inset showing colour chromaticity diagram) (b) Effect of shelf life on SEFANC and FANC emission property (c) Time trace of fluorescence emission maxima of SEFANC as compared to FANC (d) UV-Visible light absorption property of FANC, SEFANC and silica encapsulated control extending upto NIR region.

3.3.8 Light Absorption Property

Furthermore, FANC light absorption capability was confirmed by measuring the absorbance, after exposing the FANC suspension to UV-Visible light. Two absorption

bands near 270 and 350 nm, in case of control (Fig. 3.9d and inset), suggest possibility of π-π^* and n-π^* transitions. These transitions result due to sp^2 hybridized carbons, involved in C=C and C=O/C-OH groups [281], which are associated with the various phytochemicals of the leaf extract. However, this spectrum is slightly shifted towards blue region as a result of quantum confinement [282], pertaining to small size of Atacamite nanoclusters. Apart from this, FANC revealed weak near infrared absorption in the region between 600-1000 nm, as shown in figure 3.9d. The broad absorption peak is probably due to polydispersity [278] of Atacamite nanoclusters. Furthermore, absorption ranging from ~600-1000 nm bands, may correspond to metal-ligand vibrations, which arises due to slight mixing of p and d orbitals. This gives rise to d-d type absorption spectra which is characterized by a small molar extinction coefficient (calculated to be ε= 176.3 L $moles^{-1}$ cm^{-1}). However, the formation of SEFANC resulted in red-shifted and improved absorbance maxima (900 nm, Fig. 3.9d) as compared to FANC (absorption maxima ~780 nm). No absorption band is observed, corresponding to silica encapsulated control in NIR region. The improvement in SEFANC absorbance band, in the NIR region can occur due to FANC aggregation within the silica shell, also visible in the TEM analysis (Fig. 3.6a). The other likely reason for the enhanced NIR absorbance is formation of oxide layer over FANC, as confirmed by the XPS analyses (Fig. 3.7a). The generation of SPR band over fluorescent metal nanoclusters was earlier observed by Karali et al. [100] due to the presence of a semiconducting metal oxide layer on the surface.

3.4 Biological Applications of SEFANC

3.4.1 MTT Assay and Cellular Imaging

SEFANC's were tested for cellular viability on Drosophilasalivary gland tissues using [3-(4,5-dimethylthiazol-2-yl)-2,5 diphenyltetrazolium bromide] (MTT) prior to imaging. The MTT assay revealed ~67 % to 47 % cell viability (Fig. 3.10) on exposure to 0.1 mg/mL to 0.5 mg/mL SEFANC, respectively as compared to untreated control. The result indicates that SEFANC can be used in the area of tissue imaging and photothermal therapy.

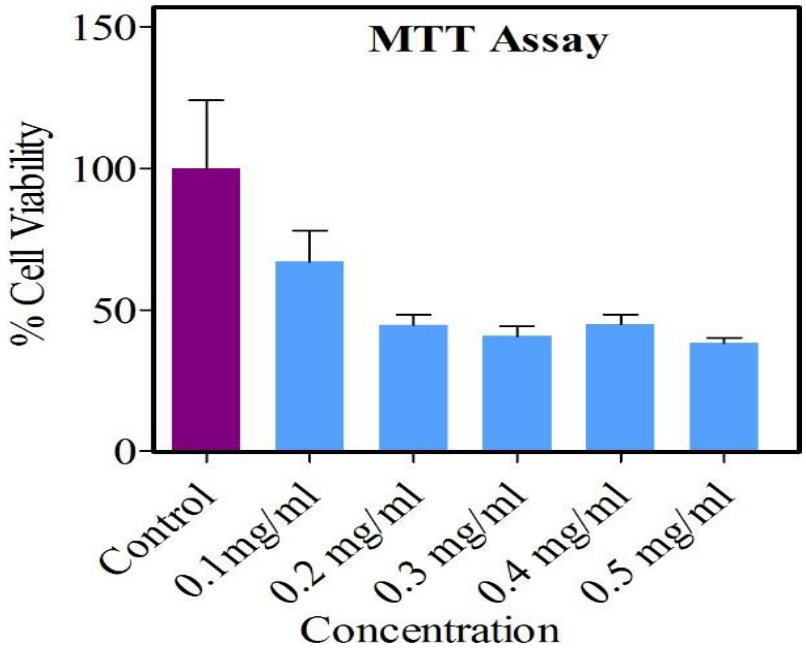

Figure 3.10 Drosophila salivary gland tissue viability test on exposure to SEFANC.

3.4.2 Drosophila Salivary Gland Tissues Imaging

Owning to biocompatibility and fluorescence property, the application of SEFANC in the area of bioimaging needs to be examined, which was performed by Drosophila salivary gland tissues imaging.

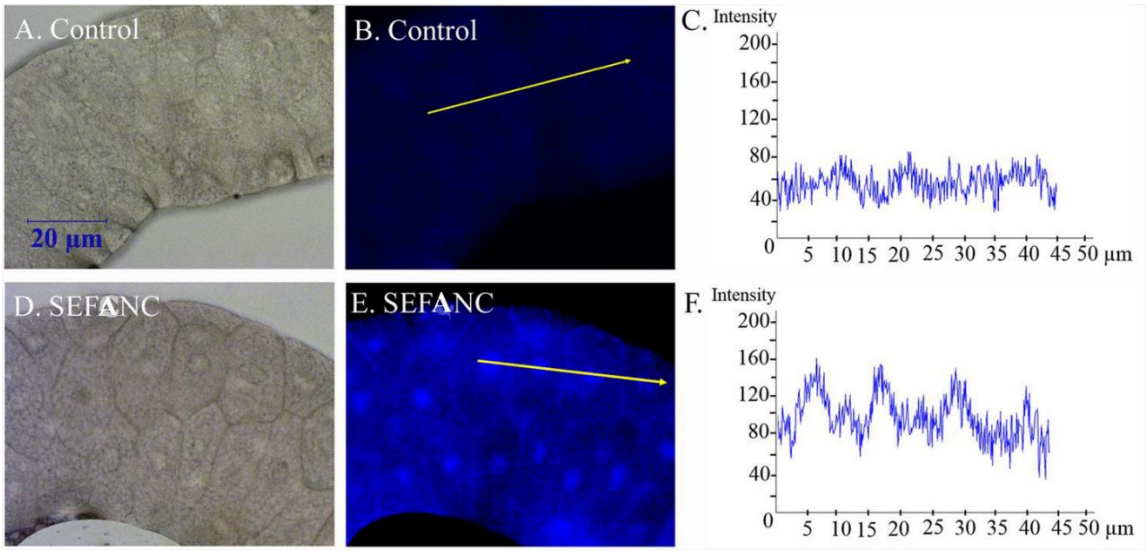

Figure 3.11 Bright field and fluorescence images of Drosophila salivary gland tissues (a) bright field image of salivary gland tissue (negative control) (b) fluorescence images (negative control),(c) fluorescence intensity (negative control) (d) bright field image (SEFANC stained), (e) fluorescencent image (SEFANC stained) and (f) fluorescence intensity from the SEFANC stained tissues.

The bright-field and fluorescence images of the SEFANC stained as well as phosphate buffer saline treated (negative control) *Drosophila* salivary gland tissue (Fig. 3.11) were acquired. The bright field images of SEFANC treated cells revealed intact hexagonal cells (Fig. 3.11d), with central nuclei as compared to the negative control (Fig. 3.11a). Further, the SEFANC stained cells manifested 1.7 times more bright blue colored (Fig. 3.11e and Fig. 3.11f) fluorescent images as compared to the negative controls (Fig. 3.11b and Fig. 3.11c).

3.4.3 Photothermal Heat Generation and Thermal Stability

The presence of 600-1000 nm absorption bands in FANC/SEFANC can be used to convert NIR light to heat, which has potential application in hyperthermia treatment. Upon NIR (975 nm) exposure, the temperature of the FANC suspension has increased from 29 ^{o}C to 42 ^{o}C (Fig. 3.12a), which is 9 ^{o}C higher than DI water ($T_{max} \approx 34$ ^{o}C). Similarly, temperature rise in the case of SEFANC suspension was found to be ~50 ^{o}C, which is ~8 ^{o}C higher than FANC. Interestingly, the photothermal conversion efficiency (*Appendix* A5) in the case of SEFANC is calculated to be 20.7 %. Such temperature rise is sufficient to induce cell death, comparable or better than other photothermal agents, used for *in Vitro* and *in Vivo* studies [283-285]. The possibility of heat generation from pure silica nanoparticle (control), examined by exposing the former to NIR light. Interestingly, the temperature rise was not significant as compared to FANC. This finding can be further strengthened from the fact that there was no light absorption in the NIR band for pure silica encapsulated control, as mentioned earlier. The change in temperature (ΔT) for SEFANC (~16 ^{o}C is slightly higher in comparison to FANC (~13 ^{o}C) which is quite high as compared to silica nanoparticle (~6.7 ^{o}C) and deionized water (~5.5 ^{o}C).

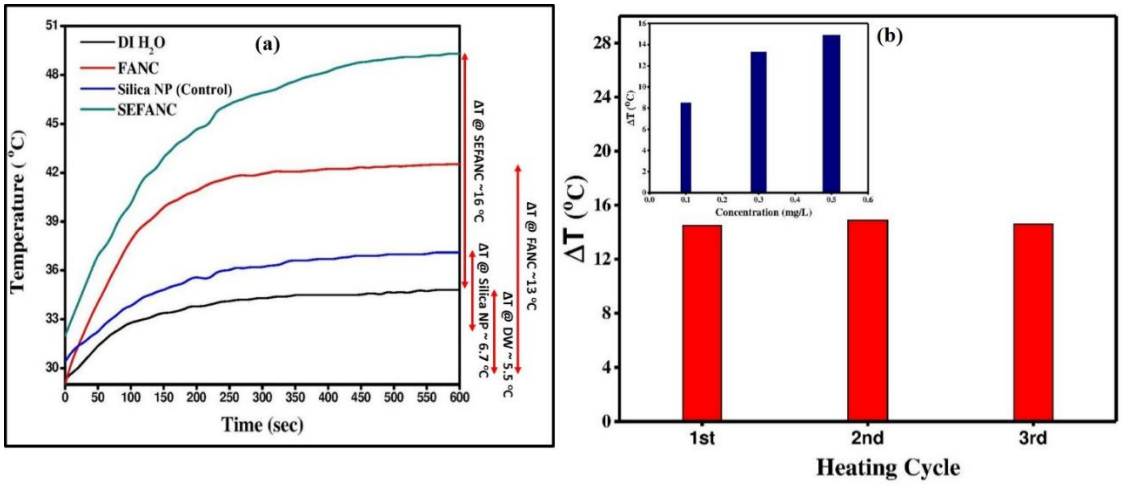

Figure 3.12 (a) NIR induced heat generation by DI water, FANC, pure silica nanoparticles (control) and SEFANC (b) Thermal stability of SEFANC upon NIR exposure at different heating cycles. Inset shows change in temperature for different concentrations of SEFANC.

The heat generation capacity was also investigated by exposing different concentrations (0.1, 0.3 and 0.5 mg/mL) of SEFANC with NIR radiation (500 mW), for 10 min. Results clearly demonstrate the highest temperature change ($\Delta T \approx 14.9$ ºC) in case of 0.5 mg/mL concentration and least ($\Delta T \approx 8.5$ ºC) for 0.1 mg/mL concentration of SEFANC (Fig. 3.12b inset). Nevertheless, even with this small temperature change ($\Delta T \approx 8.5$ ºC), cell death is possible, due to the SEFANC and radiation effect. Furthermore, studies were performed to evaluate the thermal stability of SEFANC, as shown in figure 3.12. Interestingly heat generation capability of the developed SEFANC is found to be excellent, even after three heating cycles, indicating good thermal stability.

3.4.4 *In Vitro* Photothermal Studies

NIR light can penetrate thick tissues (~few mm) and therefore, its use for real time application in photothermal therapy was examined by incubating the nanoclusters with osteosarcoma MG-63 cells. After 4h of incubation with SEFANC, the morphology of MG-63 cells is observed to be intact (Fig. 3.13a & c). However, a notable change in the morphology of these cells is observed by

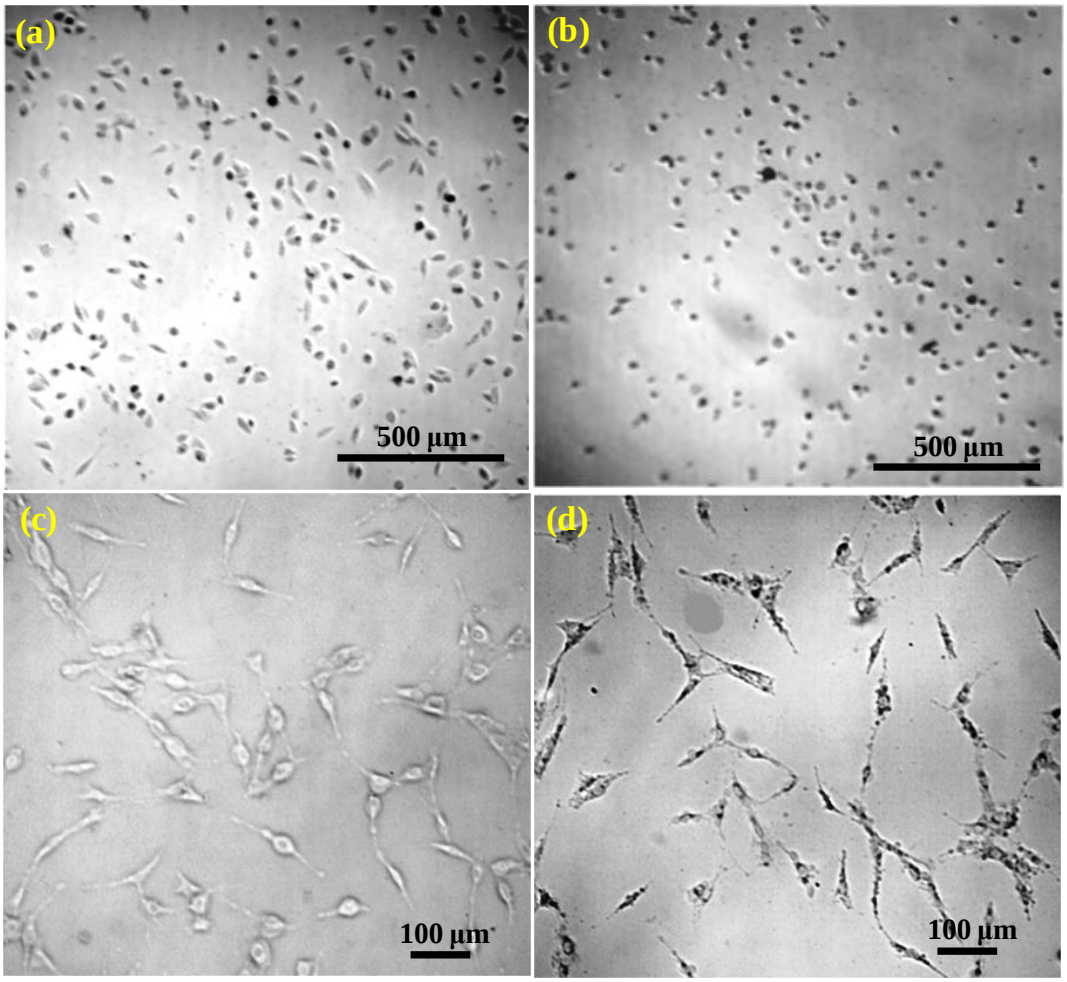

Figure 3.13 (a) Bright field images demonstrating the morphology of osteosarcoma MG-63 cells (elongated) after incubation with SEFANC (0.1 mg/mL)and (b) The drastic change in cell morphology (rounded) after combined treatment of NIR and SEFANC-(c) A closer view of SEFANC treated cells (positive control) revealing the intact morphology. (d) A closure view of cells, after combined treatment with SEFANC and NIR, suggests the cell destruction.

the combined treatment of SEFANC and NIR light (Fig. 3.13b). A closer view suggests that the cells appear to be fragmented (Fig. 3.13d). It needs to be mentioned here that the morphology of the treated cells was examined without washing with PBS. It has been observed in earlier experiments (data not presented) that the cells were washed away with PBS, which indicates that cell death occurs due to the combined treatment of SEFANC and NIR light.

3.4.5 Viability of MG-63 Cells and Photothermal Analyses

The MTT assay was performed on MG-63 cells at different SEFANC concentrations as shown in figure 3.14a. The MTT assay was performed on two groups of MG-63 cells. The first group comprised of MG-63 cells incubated with different concentration of SEFANC but not exposed to NIR light (dark). While, the second group consisted of MG-63 cells incubated with various concentration of SEFANC and exposed to NIR light. The data shows decreased cellular viability with the increase in SEFANC concentration under dark conditions. Although, it was found that at concentration below 0.3 mg/mL of SEFANC, ~70% MG-63 cells were viable. On the contrary,

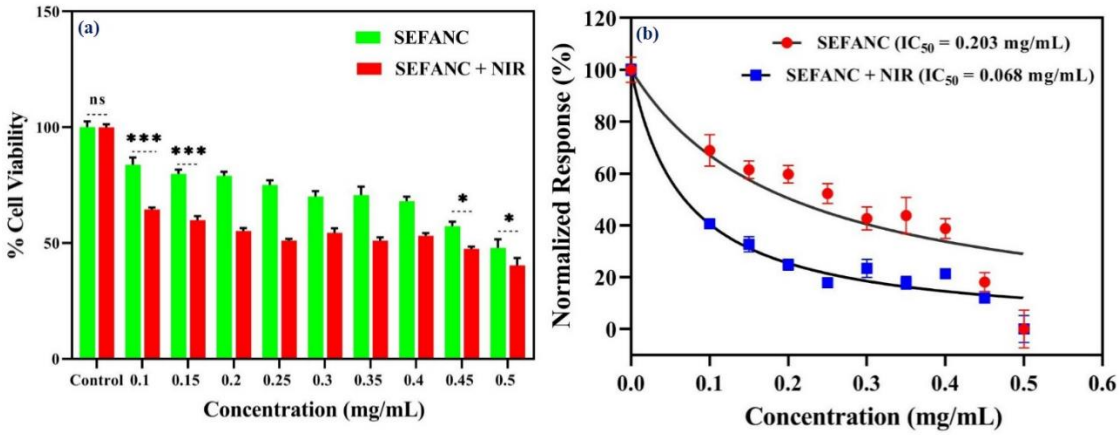

Figure 3.14 (a) Viability of MG-63 cells upon exposure to (SEFANC) and (SEFANC + NIR) doses. Two-way ANOVA was performed by Tukey's multiple comparison test for statistical differences (*p < 0.05, ***p < 0.005, ***p < 0.0001, ns-non significant). (b) IC_{50} analysis of MG-63 cells on exposure to (SEFANC) and (SEFANC+NIR).

the batch of MG-63 cells exposed to NIR light for 5 min shows decreased cellular viability as compared to their counterparts. It is important to note that even at small exposure to SEFANC with 5 min of NIR radiation, the overall cellular viability decreases by ~45 % due to synergistic effect of SEFANC and NIR radiation. Two way ANOVA analyses also suggests significant (P < 0.0001) reduction in cell viability upon NIR exposure to MG-63 cells, incubated with lower concentration of SEFANC. Furthermore,

the half maximum inhibition concentration (IC_{50}) of SEFANC (IC_{50}) was evaluated in accordance with published literature [268, 286] and found to be ~0.2 mg/mL and ~0.068 mg/mL under dark and NIR irradiation condition, respectively (Fig. 3.14b).

3.5 Magnetic behavior of Atacamite nanoclusters

Atacamite behaves as a frustrated magnet with no regular magnetic orientation. As far as the earlier studies on the magnetic properties of Atacamite are concerned, it has been carried out using microcrystalline phase which revealed its antiferromagnetic nature. However, magnetic transitions at sub-nanoscale level are interesting to examine. DC susceptibility measurement, using a commercial SQUID magnetometer, reveals the paramagnetic behavior of Atacamite nanoclusters in low (0.1 T, Fig. 3.15a) and high magnetic fields (1T) over entire temperature range (0-300K) due to overlapping of ZFC-FC curve. Negative Curie Weiss temperature [287] obtained by linear extrapolation of high-temperature data, following Curie Weiss law [288] (x^{-1} Vs. T-Θ_{cw}), support well with the antiferromagnetic nature of Atacamite. However, the second slope of curie Weiss curve has an "x" intercept at origin, due to the development of paramagnetism in the developed nanoclusters (Fig. 3.15b). Paramagnetism is attained due to the formation of small-sized single phase crystals with long range magnetic ordering [289, 290]. Such type of result is also observed in the case of dilute magnetic semiconductors having coating of thin metal oxide film over the nanostructures. Hence, the formation of a thin film of CuO over Atacamite nanostructures is again ascertained. Linearity in isothermal magnetization analysis at room temperature (Fig. 3.15c) reveals the dominance of anti-ferromagnetism in the nanoclusters. However, with the decrease in temperature up to 2K, there is a slight development of ferromagnetic to superparamagnetic interaction, supplemented by very narrow hysteresis curve and saturation (Fig. 3.15c inset), The alignment of atomic spins in same direction at very low-temperature (2K) can be the

probable reason for the development of Ferro or superparamagnetic interaction, unlike random orientation at room temperature yielding antiferromagnetic property [291]. Since Atacamite is not intrinsically ferromagnetic but it's appearance in the prepared clusters can be presumed by one or combination of several effects such as, doping of Mn, Fe etc. (found in M.oleifera leaf extract), surface defects, segregation of clusters, participation of 3d ions, and surface modification by thiolate ligands originating from plant protein, etc. [289]. In addition, the lower magnitude of X-intercept of linear extrapolated region of arrot plot (Fig 3.15d) revealed the formation of small ferromagnetic interaction in anti-ferromagnetic Atacamite nanoclusters at lower applied magnetic field. It is important to mention that the development of ferromagnetism at lower applied field most likely suppressed by larger concentration of anti-ferromagnetism in the prepared nanostructures [290]. The development of small amount of magnetic saturation in the Atacamite nanoclusters is not sufficient enough to be used in any biomedical application however; its frustrated magnetic behavior can be harnessed in various applications such as MRI contrasting agent, magnetic hyperthermia, if improvised extensively.

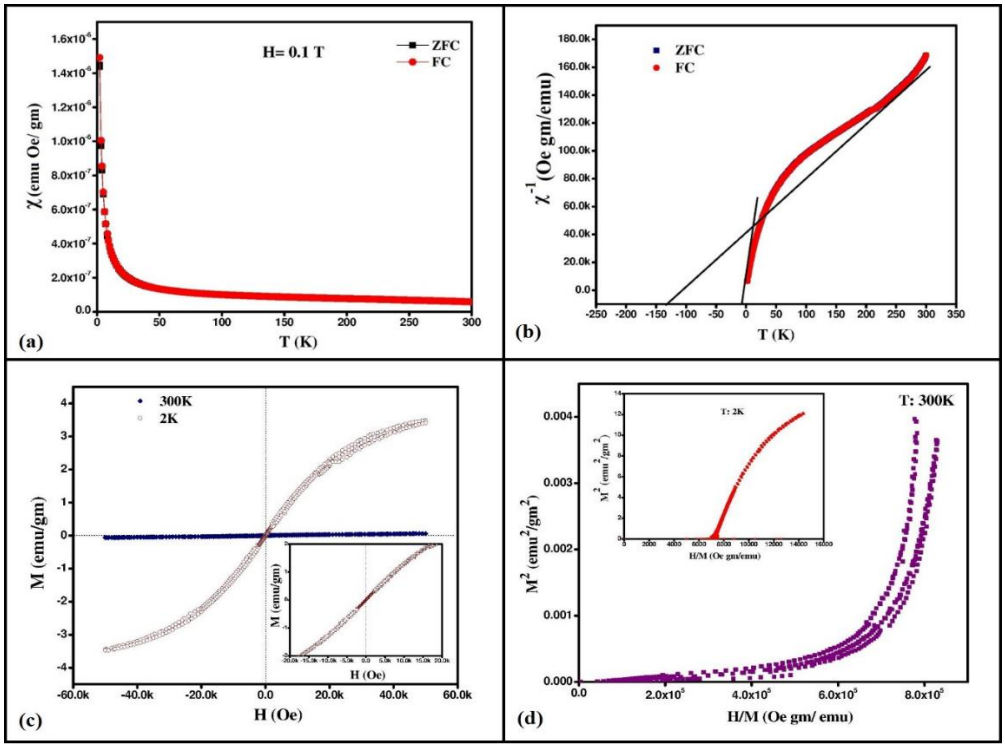

Figure 3.15 (a) DC susceptibility measurement at 0.1 T (b) Inverse susceptibility diagram showing antiferromagnetic as well as paramagnetic behavior of Atacamite (c) Isothermal magnetization curve at room temperature as well as 2K (d) arrot plot showing antiferromagnetic behavior of Atacamite nanoclusters.

3.6 Conclusions

In conclusion, we demonstrated the synthesis of Atacamite nanocluster using *M. oleifera* leaf extract. The synthesized nanocluster exhibited dual band-gap (indirect 2.5eV, direct band gap of 3.9 eV) and is inherently non-fluorescent in nature. In this work, using the fluorescent ligand, present in the *M. oleifera* leaf extract, Atacamite cluster are rendered fluorescent and used for Drosophila salivary gland tissue imaging. The FANC colloidal stability, emission output, and quantum yield are demonstrated to improve significantly with silica encapsulation, besides its capability to absorb NIR light and produce heat. Furthermore, developed SEFANC displayed the appreciable potentiality to induce osteosarcoma cell death on NIR exposure due to the heat generation.